International Journal of Non-Linear Mechanics 76 (2015) 120–134

Contents lists available at ScienceDirect

International Journal of Non-Linear Mechanics

journal homepage: www.elsevier.com/locate/nlm

Large deformation mechanics of a soft elastomeric layer under compressive loading for a MEMS tactile sensor application

Kourosh M. Kalayeh, Panos G. Charalambides *

Department of Mechanical Engineering, The University of Maryland, Baltimore County, Baltimore, MD 21250, United States

ARTICLE INFO

Article history:
Received 9 February 2015
Received in revised form
8 June 2015
Accepted 9 June 2015
Available online 17 June 2015

Keywords:
Analytical model
Mooney–Rivlin
Layer
Capacitance tactile sensor
Finite element
Comparisons

ABSTRACT

The study is motivated by the need to develop highly sensitive tactile sensors for both robotic and bionic applications. The ability to predict the response of an elastomeric layer under severe pressure conditions is key to the development of highly sensitive capacitive tactile sensors capable of detecting the location and magnitude of applied forces over a broad range of contact severity and layer depression. Thus, in this work, a large deformation Mooney–Rivlin material model is employed in establishing the non-linear mechanics of an elastomeric layer of finite thickness, subjected to uniform displacement of controlled compression. Thus, an analytical non-linear model for the above described problem which is validated numerically via the method of finite elements is developed. Two dimensional, plane strain conditions of an infinitely long and of finite thickness elastomeric layer are assumed. The layer is subjected to a uniform vertical large displacement with symmetry conditions applied at the contact center. Cauchy normal and shear stress profiles as well as displacement profiles are established over a broad range of a layer compression including up to 40% of layer thinning. The model allows for the determination of the non-linear relationship between the relative separation of embedded conducting electrodes and thus the sensor capacitance during touch, to the force magnitude of the force concentrated at the symmetry plane or sensor center. The current model is expected to further improve the sensitivity and range of polymeric tactile sensors currently under development (Charalambides and Bergbreiter, 2013) [1]. As shown elsewhere (Kalayeh et al., 2015) [2], capacitance–force model predictions are found to be in remarkable agreement with experimental measurements for a broad family of self-similar pressure sensors.

1. Introduction

The development of robust tactile sensor technologies has received ample attention over the last three decades [3–11]. Initially driven by the need to develop sensitive robotic skin that would enhance a robots sense of grasping and touch, flexible tactile sensors are more recently being considered in the development of smart human like skin that would eventually be integrated into the human nervous system thus advancing bionic technologies. For example, in 2005 and 2006, J. Sulivan and C. Mitchel who have lost their arms in life changing accidents were the first man and woman to receive bionic arms.[1] They have since been able to control their bionic arm and manipulate objects, thus restoring a sense of normalcy in their daily lives. While the above examples give a glimpse of the transformative potential of the evolving tactile sensor technologies, ample examples of the use of specialized micro-sensor devices can be found in robotic systems [12,13], medical tools and devices used during surgery and other medical purposes [14,15].

In accordance with Lee and Nicholls [16] a tactile sensor is, "a device or system that can measure a given property of an object or contact even through physical contact between the sensor and the object". This study focuses on the modeling and development of tactile sensors capable of measuring the contact pressure load between the sensor and an object. The ultimate goal is to expand the work presented in this study as needed to assess normal and shear force magnitudes as well as their position and the shear direction. Such a sensor can then be used both in robotic applications as well as in the development of "smart" artificial skin mimicking human perception with grasping capabilities. For the latter type of applications, scalability, flexibility, and stretchability are important characteristics for skin-like sensors [17].

In recent years, Microelectromechanical systems (MEMS) have been integrated into tactile sensing technology, and become a key feature in tactile sensors developments. Many MEMS based tactile sensors have been designed and fabricated [1,18–21]. In these sensors, silicon-diaphragm structures are frequently used for measuring contact forces [22–25]. But in general, silicon based devices do not provide enough stretchability and flexibility.

* Corresponding author.
E-mail addresses: kourosh2@umbc.edu (K.M. Kalayeh), panos@umbc.edu (P.G. Charalambides).

[1] http://www.ric.org/research/centers/bionic-medicine/.

http://dx.doi.org/10.1016/j.ijnonlinmec.2015.06.005
0020-7462/

Thus, flexible substrates of various polymer-based materials, such as parylene, polyimide (PI), or polydimethlysiloxane (PDMS), were proposed as the substrates for flexible sensors.

A typical conductive polymer-based tactile sensor consists of a flexible, conductive gel or elastomer capable of sensing tactile information with the aid of patterned electrodes for sensor read-out. The electrodes are usually embedded in gel (PDMS) [1,18,20,21,26,27] in pair arrangements for sensor capacitance measurements. As established elsewhere [28,29] the capacitance between two electrodes is proportional to the electrode over-lapping area while inversely proportional to the spacing distance between electrodes. Deformations induced by surface contact normal and shear stresses in the proximity of the electrode gap cause changes both in the electrode overlapping area and the electrode spacing distance. As a result, the deformed sensor outputs a new capacitance. Thus, the capacitance change could be used to identify the location, magnitude and direction of the applied loads. However, in doing so, one is required to solve an inverse problem that may not have a unique solution and may be difficult to attempt especially under large deformation, large strain conditions.

In light of the above, modeling of tactile sensors has not kept pace with the rapid advances in tactile sensor fabrication. In [30], Kumar et al. developed an analytical model for capacitive tactile sensors based on a stress inversion method. They calculated the displacements of embedded features in a polymeric matrix with the aid of an Optical Coherence Tomography (OCT) device and then used fundamentals of elasticity to derive the related stress/strain fields. In their approach they modeled PDMS as linear elastic material which is a limiting assumption. In 2011, D'Amore et al. [31] proposed a tactile sensor prototype based on LED (Light Emitting Diode)-phototransistor. They also modeled the relationship between the applied force and phototransistor measurements using neural network approach. Later on, in 2012, De Maria et al. derived an analytical model based on proposed sensor prototype in [31] by approximating the elastic layer with a single elastic beam with elliptical cross section [32]. In 2013, they enhanced their approximated analytical model to overcome some of its limitations like the model inability to capture the contact force applied in a direction other than the radial direction [33]. Lee et al. developed a simplified 3D analytical model for capacitive tactile sensors in [34], like in previous works, they limited their model to small deformations. In [35], Liang et al. present analytical model along with finite element simulations for capacitive tactile sensors by utilizing Ritz method and approximating the deformation field with Chebychev polynomials. Similar to [30] they model the PDMS as linear elastic material. Also in the aforementioned work the reported capacitance–force relation is limited to linear regime, i.e., small deformations. There are also some reports on using MEMS and multi-physics solvers to simulate the performance of these sensors [20].

As already mentioned, small deformation, strain conditions are often employed as needed to obtain relevant results when operating within the linear regime [36,26,27]. Invariably, such assumptions limit the reliable sensor range rendering the interpretation of sensor capacitance readings not reliable under the application of relatively large contact loads.

In order to overcome some of the above sensor design limitations, this study employs a non-linear material and kinematic model capable of capturing the polymeric layer deformation over a wide range of applied loads accounting for both material and geometric non-linearities. The premise of the study is that the relatively stiffer electrodes, during deformation, “float” within the layer like a pair of stiff wires placed in a layer of soft jello. As such, all information needed for the interpretation of capacitance change readings can be extracted from the large deformation mechanics of the elastomeric layer alone, subjected to the applied contact loads. In fact, as is shown in our other work [2], capacitance–pressure load model predictions developed as part of this effort are shown to be in remarkable agreement with experimental measurements over a wide range of applied contact sensor loading. While an analytical model for a unidirectionally compressed polymeric layer is fully developed in this study, requisite non-linear finite element studies are also presented with broad comparisons between the analytical and finite element results for up to 40% layer compression. The detailed development of both the analytical and numerical finite element models shall be presented next.

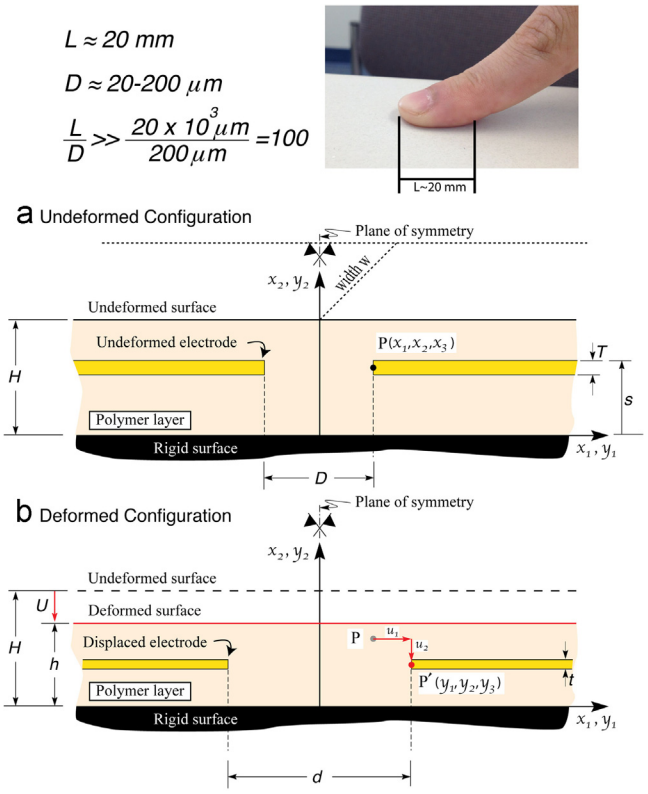

Fig. 1. A schematic of a flexible polymer layer sensor developed in [1] for contact pressure detection. The undeformed state is shown in (a) whereas the deformed state under uniform displacement conditions is shown in (b). In the model development, an infinitely long layer under plane strain condition is assumed. As shown, typical tactile contact to electrode spacing ratio is well over 100, thus, justifying the infinitely long layer approach since interested only in obtaining layer deformation in the near vicinity of the electrode gap. (For interpretation of the references to color in this figure caption, the reader is referred to the web version of this paper.)

2. Analytical model development

The analytical model developed in this study is formulated based on the polymeric sensor geometry shown in Fig. 1. Sensor design details including the materials and micro-fabrication process used can be found elsewhere [1]. The testing protocol, the extraction of experimental data and comparisons to the model predictions are presented in detail in [2]. As shown in Fig. 1, a polymeric layer of initial or undeformed thickness H is subjected to a uniform displacement U at its top surface. Using a specialized micro-fabrication process [1], conducting electrodes of higher stiffness compared to the polymer layer are introduced as horizontally embedded layers at position S from the bottom solid foundation. At its unloaded or initial position, the sensor electrodes are

aligned, symmetrically placed relative to the x_2-axis of symmetry as shown in Fig. 1. The initial electrode thickness is T and the electrode width is W spanning the entire sensor width.

The boundary value problem solved as part of the analytical model is meant to capture the deformation of the polymer layer in the absence of the relatively stiffer electrodes. As such, in this model, stiffer electrodes suspended within the softer polymer layer are assumed to displace consistent with the surrounding layer deformation. For illustrative purposes, Fig. 1 shows schematics of both the undeformed (a) and deformed (b) layer subjected to a uniform top surface displacement U. The red dashed horizontal line indicates the deformed location of the top contact surface, whereas the displaced electrodes are represented by the faded yellow layers. As shown, a point P initially located at reference position x_1, x_2, x_3 has displaced to P' marked by the current coordinates y_1, y_2, y_3. The displacement components of point P are assumed to be $u_1(x_1,x_2)$ and $u_2(x_2)$. In our layer model, these latter displacements are those obtained from the large deformation mechanics of the layer model in the absence of the electrodes thus neglecting electrode layer–polymeric layer interaction during deformation. As will be shown later on, in this study, such approach does allow for the development of useful analytical expressions governing the electrode pair gap evolution with the applied displacement which is critical in capacitance measurements and interpretation. In addition to the above, an electrode layer thinning during model deformation is also developed as a "stand-alone" problem knowing the polymeric layer stress state at the electrode position.

2.1. Layer kinematics

In light of the above, the polymeric layer mechanics model is formulated and developed using the geometry shown in Fig. 2. Given the large tactile contact area to electrode spacing ratio shown in Fig. 1, an infinitely long elastomeric layer is assumed. Furthermore, assuming uniform contact along the x_3 direction, the layer deformation takes place under plane strain conditions provided that the material properties, layer geometry and boundary conditions remain as those shown in Figs. 1 and 2 on the x_1–x_2 plane profile.

Given the above, it is assumed that the soft polymer layer in the vicinity of the electrode pair undergoes large deformations induced by a uniform displacement U during tactile contact on the top surface of the sensor as shown in Fig. 2. At the same time, Fig. 2 is also depicting that the deforming layer is assumed to be securely fixed to a rigid substrate. In the model development, a Mooney–Rivlin hyperelastic material response is used to relate true stress to true strain. Large deformation kinematics are developed consistent with the solution approach used in [37] and using the (x_1,x_2,x_3) coordinates for the reference or undeformed state and (y_1,y_2,y_3) coordinates parameterizing the deformed or current state as shown in Fig. 2. Symmetry conditions are enforced along the $x_1=0$ and $y_1=0$ axes.

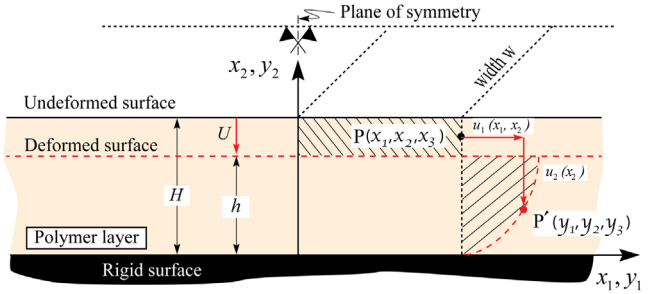

Fig. 2. The polymer layer geometry used in formulating the large deformation, large strain layer mechanics model. During deformation Point $P(x_1,x_2,x_3)$ in the reference configuration displaced to Point $P'(y_1,y_2,y_3)$ with displacement components $u_1(x_1,x_2)$ and $u_2(x_2)$ as modeled in this study.

In light of the above and by assuming that initially horizontal lines remain horizontal after deformation the following kinematics equations are derived:

$$y_1(x_1,x_2,x_3)=y_1(x_1,x_2), \tag{1a}$$

$$y_2(x_1,x_2,x_3)=y_2(x_2)=g(x_2), \tag{1b}$$

$$y_3(x_1,x_2,x_3)=y_3(x_3)=x_3, \tag{1c}$$

where $g(x_2)$ is a determined general function that depends only on x_2.

Based on the above equations the deformation gradient tensor $\tilde{F}$ can be derived as follows:

$$[F_{ij}]=\begin{bmatrix} \frac{\partial y_1}{\partial x_1} & \frac{\partial y_1}{\partial x_2} & \frac{\partial y_1}{\partial x_3} \\ \frac{\partial y_2}{\partial x_1} & \frac{\partial y_2}{\partial x_2} & \frac{\partial y_2}{\partial x_3} \\ \frac{\partial y_3}{\partial x_1} & \frac{\partial y_3}{\partial x_2} & \frac{\partial y_3}{\partial x_3} \end{bmatrix}=\begin{bmatrix} \frac{\partial y_1}{\partial x_1} & \frac{\partial y_1}{\partial x_2} & 0 \\ 0 & g'(x_2) & 0 \\ 0 & 0 & 1 \end{bmatrix}. \tag{2}$$

Consistent with Rivlin phenomenological theory, the Mooney–Rivlin hyperelastic material employed in this study should lead to isohoric deformation conditions, i.e., no change in volume allowed at any point in the solution domain. Under large deformation conditions isohoric deformation requires that

$$J=\det(\tilde{F})=\frac{\partial y_1}{\partial x_1}g'(x_2)=1, \tag{3}$$

therefore,

$$\frac{\partial y_1}{\partial x_1}=\frac{1}{g'(x_2)}, \tag{4}$$

thus by integrating the above equation one arrives at

$$\begin{aligned} y_1(x_1,x_2)&=\frac{1}{g'(x_2)}x_1+k(x_2)\\ &=f(x_2)x_1+k(x_2), \end{aligned} \tag{5}$$

where $f(x_2)=1/g'(x_2)$ is introduced for convenience and $k(x_2)$ is an arbitrary function of x_2 which will be determined through boundary conditions later on in this work.

The form of y_1 given above is derived using the adopted form for $y_2=g(x_2)$ along with the condition of isohoric deformation that applies to the Mooney–Rivlin material adopted in the study specifically. In light of Eq. (5), the kinematic equations take the form

$$y_1(x_1,x_2)=x_1f(x_2)+k(x_2), \tag{6a}$$

$$y_2(x_2)=g(x_2), \tag{6b}$$

$$y_3(x_3)=x_3. \tag{6c}$$

2.2. Boundary conditions

Due to symmetry, the points on the $x_1=0$ (symmetry axis) should remain on the same axis after deformation, i.e.,

$$y_1(0,x_2)=0. \tag{7}$$

In addition, the points on the bottom surface of the layer attached to a rigid foundation should remain stationary during the deformation, i.e.,

$$y_1(x_1,0)=x_1, \tag{8a}$$

$$y_2(x_1,0)=0. \tag{8b}$$

When enforcing symmetry condition given by Eq. (7) it follows that $k(x_2)=0$ and thus

$$y_1(x_1,x_2)=x_1 f(x_2). \tag{9}$$

The above condition further simplifies the kinematic equations as follows:

$$y_1(x_1,x_2)=x_1 f(x_2), \tag{10a}$$

$$y_2(x_2)=g(x_2), \tag{10b}$$

$$y_3(x_3)=x_3, \tag{10c}$$

with $fg'=1$. With the aid of the above equations the deformation gradient takes the form

$$\tilde{F}=\begin{bmatrix} f & x_1 f' & 0 \\ 0 & g' & 0 \\ 0 & 0 & 1 \end{bmatrix}. \tag{11}$$

The associated finger deformation tensor $\tilde{B}$ can be calculated as follows:

$$\tilde{B}=\tilde{F}.\tilde{F}^T=\begin{bmatrix} f^2+(x_1 f')^2 & x_1 f' g' & 0 \\ x_1 f' g' & g'^2 & 0 \\ 0 & 0 & 1 \end{bmatrix}. \tag{12}$$

Its inverse is then given by

$$\tilde{B}^{-1}=\begin{bmatrix} g'^2 & -x_1 f' g' & 0 \\ -x_1 f' g' & f^2+x_1^2 f'^2 & 0 \\ 0 & 0 & 1 \end{bmatrix}. \tag{13}$$

2.3. Constitutive response

The soft polymer phase is modeled using a Mooney–Rivlin hyperelastic material response. In such hyperelastic materials the stress and strains can be related through a strain energy function $\Phi(I_1,I_2,I_3)$ which is often expressed in terms of strain invariants I_1,I_2,I_3 or principal stretch ratios $\lambda_1,\lambda_2,\lambda_3$. The stain invariants can be expressed in terms of the stretch ratios as follows [38]:

$$I_1=\lambda_1^2+\lambda_2^2+\lambda_3^2, \tag{14a}$$

$$I_2=\lambda_1^2\lambda_2^2+\lambda_2^2\lambda_3^2+\lambda_3^2\lambda_1^2, \tag{14b}$$

$$I_3=\lambda_1^2\lambda_2^2\lambda_3^2. \tag{14c}$$

For incompressible materials associated with isohoric deformation, $I_3=(\lambda_1\lambda_2\lambda_3)^2=(\det(\tilde{F}))^2=J^2=1$ and consequently $\Phi=\Phi(I_1,I_2)$. While several forms of strain energy functions have been proposed in modeling various types of hyperelastic materials [39], in this study we shall employ a Mooney–Rivlin material model such that

$$\Phi=C_{10}(I_1-3)+C_{01}(I_2-3), \tag{15}$$

where C_{10} and C_{01} are material properties describing the elastic response of the material. For isotropic materials the shear and bulk modulus are defined respectively as

$$\mu_0=C_{10}-C_{01}, \tag{16a}$$

$$K_0=\frac{2}{D_1}. \tag{16b}$$

For incompressible systems $D_1=0$ and $K_0\to\infty$. In accordance with the adopted Mooney–Rivlin model the true or Cauchy stress $\tilde{\sigma}$ can be obtained as follows [38]:

$$[\sigma]=-P[I]+C_1[B]+C_2[B^{-1}]. \tag{17}$$

The above constitutive model allows us for a pressure term $-P$ as needed to properly account for incompressibility conditions. In the above equation $C_1=C_{10}$ and $C_2=C_{01}$ whereas $[B]$ and $[B^{-1}]$ are the finger deformation tensor and its inverse given by Eqs. (12) and (13) respectively.

2.4. The Cauchy and Piola–Kirchhoff stresses

Consistent with Eq. (17) and with the aid of Eqs. (12) and (13) the following expressions are obtained for the Cauchy stresses:

$$\sigma_{11}=-P+C_1(f^2+(x_1 f')^2)+C_2 g'^2, \tag{18a}$$

$$\sigma_{12}=(C_1-C_2)x_1 f' g', \tag{18b}$$

$$\sigma_{22}=-P+C_1 g'^2+C_2(f^2+x_1^2 f'^2). \tag{18c}$$

In enforcing local equilibrium in the reference state or undeformed state, the 1st Piola–Kirchhoff tensor $\tilde{T}$ is required. The latter tensor can be expressed in terms of the Cauchy stress tensor $\tilde{\sigma}$, the deformation gradient $\tilde{F}$, and $J=\det\tilde{F}$ as follows:

$$\tilde{T}=J\cdot\tilde{F}^{-1}\cdot\tilde{\sigma}. \tag{19}$$

Thus the components of the above 1st Piola–Kirchhoff stress tensor are derived and take the following form:

$$T_{11}=g'([-P+C_1(f^2+(x_1 f')^2)+C_2 g'^2]-(C_1-C_2)(x_1 f')^2), \tag{20a}$$

$$T_{12}=-x_1 f'[-P+C_1 g'^2+C_2(f^2+x_1^2 f'^2)]+(C_1-C_2)x_1 f' g'^2, \tag{20b}$$

$$T_{21}=(C_1-C_2)x_1 f', \tag{20c}$$

$$T_{22}=f[-P+C_1 g'^2+C_2(f^2+x_1^2 f'^2)]. \tag{20d}$$

As evident by the form of the equations both Cauchy and Piola–Kirchhoff stresses are given in terms of the unknown functions $f(x_2)$ and $g'(x_2)$, the pressure $P(x_1,x_2)$ and material constants C_1 and C_2.

2.5. Enforcing local equilibrium

In the absence of body forces, the local equilibrium equations enforced in the reference or undeformed state are given by $T_{ki,k}=0$ which can be expanded as follows:

$$\frac{\partial T_{11}}{\partial x_1}+\frac{\partial T_{21}}{\partial x_2}=0, \tag{21a}$$

$$\frac{\partial T_{12}}{\partial x_1}+\frac{\partial T_{22}}{\partial x_2}=0. \tag{21b}$$

When combining Eqs. (20a)–(20d) and equilibrium equations (21), one arrives at the following consistency equations in $P(x_1,x_2)$, $f=1/g'$, f', and f'':

$$\frac{\partial P}{\partial x_1}=2C_2 x_1 f'^2+(C_1-C_2)x_1 f f'', \tag{22a}$$

$$\frac{\partial P}{\partial x_2}=-(C_1+C_2)\frac{f'}{f^3}+(C_1+C_2)x_1^2 f' f''+2C_2 f' f. \tag{22b}$$

By differentiating (22a) with respect to x_2 and (22b) with respect to x_1 it can be shown that

$$\frac{\partial}{\partial x_2}\frac{f''}{f}=0, \tag{23}$$

therefore,

$$\frac{f''}{f}=A, \tag{24}$$

where A is a constant of integration. An expression for the pressure $P(x_1,x_2)$ can be obtained in terms of the reference coordinates, $f(x_2)$ and $f'(x_2)$ by combining Eqs. (22) and (24), such that

$$P=\frac{(C_1-C_2)}{2}Ax_1^2f^2+\frac{(C_1+C_2)}{2}\frac{1}{f^2}$$
$$+C_2(x_1^2f'^2+f^2)+B, \tag{25}$$

where A and B are constants to be determined.

2.6. Enforcing remaining boundary conditions

In accordance with the deformation schematic shown in Fig. 3, the following boundary conditions apply

(i) *Kinematic geometric conditions*

$$\text{on } x_2=0 \quad y_1(x_1,0)=x_1, \tag{26a}$$
$$y_2(x_1,0)=0, \tag{26b}$$
$$\text{on } x_1=0 \quad y_1(0,x_2)=0, \tag{26c}$$
$$\text{on } x_2=H \quad y_1(x_1,H)=\lambda x_1, \tag{26d}$$

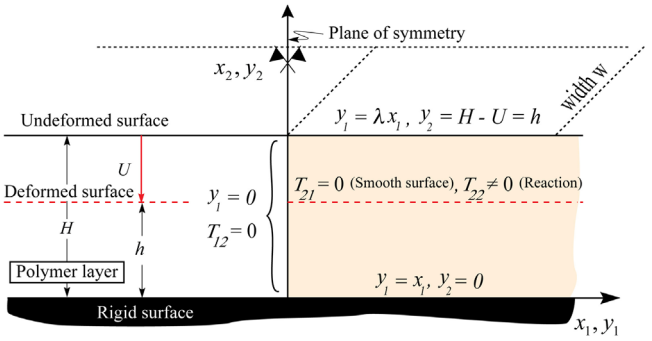

Fig. 3. Kinematic geometric and traction boundary conditions enforced in solving (24) simulating an infinitely long layer subjected to uniform compressive displacement U.

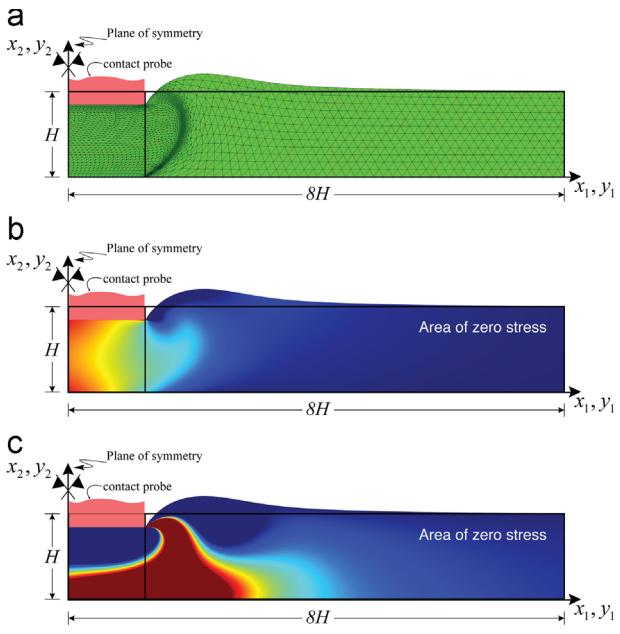

Fig. 4. (a) The deformed mesh of a finite elastomeric layer, fixed along its bottom surface and subjected to $0.05H$ uniform displacement over a finite contact probe region of length comparable to the layer thickness H. Fringe contours of (b) the 1st Piola–Kirchhoff stress component T_{11} and (c) the 1st Piola–Kirchhoff shear stress T_{12} associated with the problem solve in (a) above. Both stress components are plotted over the deformed configuration. The dark region represents region of zero stress levels. The results are obtained using COMSOL multiphysics version 5.0. with 6212 triangular elements.

$$y_2(x_1,H)=H-U=h. \tag{26e}$$

(ii) *Stress traction conditions*

$$\text{on } x_1=0 \quad \sigma_{12}(0,x_2)=0$$
$$\text{(symmetry condition)} \tag{27a}$$

$$\text{on } x_2=H \quad \sigma_{12}(x_1,H)=0$$
$$\text{(smooth contact condition)} \tag{27b}$$

(iii) *Global equilibrium in the long layer direction*

As will become apparent later on in this study, global force equilibrium in the x_1-direction yields critical information regarding the build-up of pressure in the area of interest close to the symmetry plane beneath the sensor contact region. Enforcing such a condition on an infinitely long layer subjected to a constant compression along its top surface would be difficult if not impossible, since it will require information on the non-zero T_{11} stress component acting on a vertical line as $x_1\to\infty$ while also requiring the entire profile of $T_{21}(x_1,0)$ as $x_1\to\infty$. Meanwhile, in such a case, unrealistically high pressures are expected to build in the proximity of the symmetry plane as the layer compresses and material is forced outwards from the symmetry plane, over an increasingly smaller and smaller region with increasing layer compression. Thus, such a case would not be of interest to the modeling and design of pressure sensors for which pressure is applied over a finite sensor contact surface.

In aligning our model with the pressure sensor geometric conditions, global equilibrium in the x_1-direction is applied for a layer that its length is sufficiently long when compared to the sensor contact area such that the right edge of the layer remains traction free. An example of such a system is shown in Fig. 4 which shows the deformed mesh and contours of the T_{11} and T_{12} stress components plotted on the deformed layer configuration. The results reported in the above figure were obtained using the Abaqus finite element software and the COMSOL multi-physics software package for verification. The finite element modeling is discussed in more detail later on in the study. As shown in Fig. 4, both the shear and normal stresses appear to diminish rapidly beyond the contact region over which the uniform displacement is applied on the top surface and become zero on the right vertical face of the layer. The above results remain consistent with those reported in Figs. 6 and 7 where contours and profiles of the shear stress components are reported for a layer subjected to finite contact.

In such a system, the fields dominating the region in the vicinity of the contact zone remain of interest and relevance to the sensor design and most importantly can be captured by the model proposed herein. In light of the above, and consistent with Fig. 5, global equilibrium in the x_1 direction can be enforced using the free body diagram of the symmetric right half of the layer extending over a sufficiently large length x_c compared to the contact region. Thus, under a smooth contact condition, i.e., $T_{21}(x_1,H)=0$, and with the aid of Fig. 5, the global equilibrium in the x_1 direction takes the form

$$\sum F_1=0$$
$$\Rightarrow \int_0^H T_{11}(0,x_2)\,dx_2+\int_0^L T_{21}(x_1,0)\,dx_1$$
$$+\int_L^{x_c} T_{21}(x_1,0)\,dx_1+\int_0^H T_{11}(x_c,x_2)\,dx_2=0. \tag{28}$$

Again, consistent with Fig. 5, $T_{21}(x_1,0)\to 0$, i.e., it vanishes in $L\le x_1\le x_c$ while also $T_{11}(x_c,x_2)=0$ at the traction free end of the

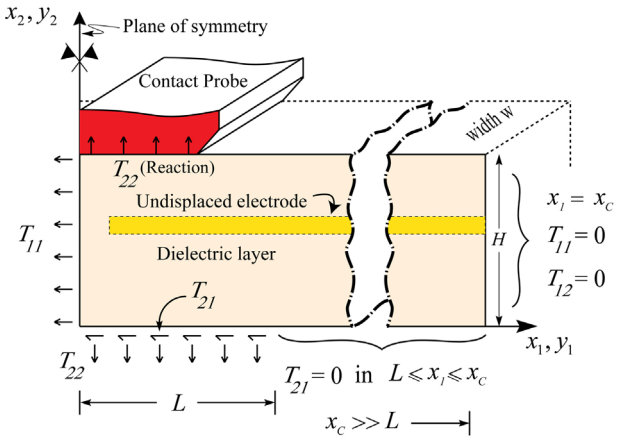

Fig. 5. Schematic of the right hand side symmetric domain used in enforcing global force equilibrium in the x_1 direction. In doing so, the 1st Piola–Kirchhoff stresses are employed in enforcing equilibrium in the reference or undeformed state.

layer. Thus, the above equation can be reduced as follows:

$$\int_0^H T_{11}(0,x_2)\,dx_2 + \int_0^L T_{21}(x_1,0)\,dx_1 = 0. \tag{29}$$

Alternatively, by considering the equilibrium in the x_1 direction of a domain $(0,L)\times(0,H)$ one can also arrive at the following equation:

$$\int_0^H T_{11}(0,x_2)\,dx_2 + \int_0^L T_{21}(x_1,0)\,dx_1 + \int_0^H T_{11}(L,x_2)\,dx_2 = 0. \tag{30}$$

Since both forms of the equilibrium equations reflected in Eqs. (29) and (30) are true, it follows that

$$\int_0^H T_{11}(L,x_2)\,dx_2 = 0. \tag{31}$$

The above condition must remain true and can be used as an alternative to (29) in calculating the constant B. However, the above condition as in condition (29) still requires knowledge of L, i.e., the extent over which the shear stress $T_{21}(x_1,0)$ vanishes.

Thus, in the case of a finite contact problem of the type shown in Fig. 5, one could use either Eq. (29) or Eq. (31) in enforcing global equilibrium in the x_1 direction as required to calculate the constant B.

Furthermore, in enforcing global equilibrium, i.e., Eq. (29) one can use the current (deformed) configuration instead of the reference (undeformed) one. In the latter case the global equilibrium will take the following form:

$$\int_0^h \sigma_{11}(0,y_2)\,dy_2 + \int_0^{L'} \sigma_{21}(y_1,0)\,dy_1 = 0, \tag{32}$$

where L and L' are lengths over which the shear stresses acting at the bottom surface of the layer vanish when the loading displacement U is applied over a finite length instead of the entire layer.

Also in Eq. (26d), λ is defined as $\lambda = f(x_2 = H)$, which is the principal stretch ratio for material points at the top surface of the polymer layer.

Enforcement of the conditions in Eqs. (26) and (27) results in the following conditions on $f(x_2)$ and $g(x_2)$:

$$x_2 = 0 \rightarrow y_1(x_1,0) = x_1 \rightarrow f(0) = 1, \tag{33a}$$

$$x_2 = 0 \rightarrow y_2(x_1,0) = 0 \rightarrow g(0) = 0, \tag{33b}$$

$$x_2 = H \rightarrow y_1(x_1,H) = \lambda x_1 \rightarrow f(H) = \lambda, \tag{33c}$$

$$x_2 = H \quad \rightarrow y_2(x_1,H) = h \rightarrow \quad g(H) = h, \tag{33d}$$

$$x_2 = H \quad \rightarrow \sigma_{12}(x_1,H) = 0 \quad \rightarrow f'(H) = 0. \tag{33e}$$

For physically admissible kinematics under compression, $y_1(x_1,x_2)$ is expected to increase with x_2 for a fixed x_1. Therefore since $y_1 = x_1 f(x_2)$, the function $f(x_2)$ must monotonically increase with x_2 consistent with the deformation profile shown in Fig. 2. In light of the above observation and in light of Eq. (24) and conditions (33c) and (33e) above, it can be concluded that the constant A must be negative. With the above in mind let

$$A = -\alpha^2, \tag{34}$$

where α is any real number.

Then Eq. (24) will yield to a general solution which under the boundary conditions (33a) and (33c) above takes the form

$$f(x_2) = \cos(\alpha x_2) + \left(\frac{\lambda - \cos(\alpha H)}{\sin(\alpha H)}\right)\sin(\alpha x_2). \tag{35}$$

Enforcement of condition (33e) in combination with the above solution for $f(x_2)$ yields

$$\lambda = \sec(\alpha H). \tag{36}$$

By substituting λ in (35) with (36), $f(x_2)$ can be further simplified to

$$f(x_2) = \cos(\alpha x_2) + \tan(\alpha H)\sin(\alpha x_2). \tag{37}$$

Since λ represents the principle stretch ratio at top surface of the layer, under compression, λ must be greater than 1 due to extensional effects in x_1 direction caused by compression along x_2 direction. As a result the phase angle αH appearing in the above equation must be restricted to the interval $0 \leq \alpha H \leq \pi/2$. Also by combining Eq. (37) with boundary condition (33b) and using $fg' = 1$ we obtain a general expression for $g(x_2)$ as follows:

$$g(x_2) = \frac{\cos(\alpha H)}{\alpha}\left(\log\frac{1+\sin(\alpha H)}{1-\sin(\alpha H)} - \log\frac{1+\left(\tan(\alpha H) - \tan\left(\frac{\alpha x_2}{2}\right)\right)\cos(\alpha H)}{1-\left(\tan(\alpha H) - \tan\left(\frac{\alpha x_2}{2}\right)\right)\cos(\alpha H)}\right), \tag{38}$$

Enforcing condition (33d) the following non-linear equation in α is obtained:

$$H - U = h = \frac{\cos(\alpha H)}{\alpha}\left(\log\frac{1+\sin(\alpha H)}{1-\sin(\alpha H)} - \log\frac{1+\left(\tan(\alpha H) - \tan\left(\frac{\alpha H}{2}\right)\right)\cos(\alpha H)}{1-\left(\tan(\alpha H) - \tan\left(\frac{\alpha H}{2}\right)\right)\cos(\alpha H)}\right), \tag{39}$$

when dividing the above equation by H the following normalized form for αH is obtained:

$$1 - \frac{U}{H} = \frac{h}{H} = \frac{\cos(\alpha H)}{\alpha H}\left(\log\frac{1+\sin(\alpha H)}{1-\sin(\alpha H)} - \log\frac{1+\left(\tan(\alpha H) - \tan\left(\frac{\alpha H}{2}\right)\right)\cos(\alpha H)}{1-\left(\tan(\alpha H) - \tan\left(\frac{\alpha H}{2}\right)\right)\cos(\alpha H)}\right). \tag{40}$$

With the aid of the above equations, the normalized integration constants αH and AH^2 are calculated and reported in Table 1 for various U/H ratios.

2.7. Normalization

In order to be able to generate a class of self-similar solutions, independent variables defined in previous sections, i.e., length (L)

Table 1
The constant α obtained by solving the nonlinear equation (39) for different layer compression levels.

%U/H	αH	$AH^2(\times 10^{-3})$
5	0.007745108450011	0.059986704902432
10	0.010949428377488	0.119889981793739
15	0.013402082218189	0.179615807783098
20	0.015461483663554	0.239057477078347
25	0.017265407642140	0.298094301049266
30	0.018883597411389	0.356590251195417
40	0.021710142543939	0.471330289278150

and modulus (C), need to be normalized based on characteristic quantities L_C and C_C respectively.

By letting $L_C = H$ and $C_C = C_1$ respectively a normalized pressure $\hat{P}$ and the Cauchy stress components $\hat{\sigma}_{11}, \hat{\sigma}_{22}, \hat{\sigma}_{12}$ are obtained as follows:

$$\hat{P} = \frac{P}{C_c} = \hat{C}_2 \hat{x}_1^2 (\hat{f}')^2 + \frac{(\hat{C}_1 - \hat{C}_2)}{2} \hat{A} \hat{x}_1^2 \hat{f}^2 + \frac{(\hat{C}_1 + \hat{C}_2)}{2} \frac{1}{\hat{f}^2} + \hat{C}_2 \hat{f}^2 + \hat{B}, \tag{41}$$

$$\hat{\sigma}_{11} = \frac{\sigma_{11}}{C_c} = -\hat{P} + \hat{C}_1 (\hat{f}^2 + (\hat{x}_1 \hat{f}')^2) + \frac{\hat{C}_2}{\hat{f}^2}, \tag{42a}$$

$$\hat{\sigma}_{22} = \frac{\sigma_{22}}{C_c} = -\hat{P} + \hat{C}_2 (\hat{f}^2 + (\hat{x}_1 \hat{f}')^2) + \frac{\hat{C}_1}{\hat{f}^2}, \tag{42b}$$

$$\hat{\sigma}_{12} = \frac{\sigma_{12}}{C_c} = (\hat{C}_1 - \hat{C}_2) \hat{x}_1 \frac{\hat{f}'}{\hat{f}}, \tag{42c}$$

where henceforth the "hat" shall represent normalized quantities.

The integration constant B shall be determined next.

2.8. On the integration constant B

The integration constant B can be calculated using Fig. 5 in conjunction with Eqs. (29) or (32), i.e.,

$$\int_0^H T_{11}(0, x_2)\, dx_2 = -\int_0^L T_{21}(x_1, 0)\, dx_1. \tag{43}$$

By combining Eqs. (20a) and (20c) with Eqs. (25), (37) and (38) and evaluating them at $x_1 = 0$ and $x_2 = 0$ respectively one arrives at

$$T_{11}(0, x_2) = \frac{1}{f} \left(\frac{(C_2 - C_1)}{2} \frac{1}{f^2} + (C_1 - C_2) f^2 - B \right), \tag{44a}$$

$$T_{21}(x_1, 0) = (C_1 - C_2) \alpha \tan(\alpha H) x_1. \tag{44b}$$

By integrating (44a) and (44b) from 0 to H and 0 to L respectively and using Eq. (43) the constant B can be calculated as follows:

$$B = \frac{\mu}{n \cos(\alpha H)} \left(\frac{-1}{4} \left(\frac{1}{2} \sin(2\alpha H) + n \cos^3(\alpha H) \right) + \tan(\alpha H) \left(1 + \frac{1}{2} \alpha^2 L^2 \right) \right), \tag{45}$$

with μ being defined as the shear modulus consistent with Eq. (16) and n introduced as

$$n = \log \left(\frac{2 \sin\left(\frac{\alpha H}{2}\right)}{\cos\left(\frac{\alpha H}{2}\right) - \sin\left(\frac{\alpha H}{2}\right)} + 1 \right). \tag{46}$$

As mentioned in Section 2.6 and indicated in Eq. (45), in order to calculate the constant B, one needs to know the length L, over which the shear stress acting at the bottom surface of the layer vanishes when the loading is applied over a finite length rather than the entire length of the layer.

While in the analytical model developed in this work, the displacements u_1 and u_2 are independent of the constant B, the stress component σ_{22} and pressure P do depend on B, consistent with Eqs. (18c) and (25) respectively. Thus, in the stress comparison studies presented later on in this work, the constant B is calculated using large deformation finite element results. As discussed elsewhere [2], in calculating the constant B which controls the built up pressure P and σ_{22} stress component and thus the probe force resultant F one may need to either conduct specific finite element studies through which the length L can be determined or develop approximate empirical methods that yield appropriate pressure outcomes.

While such efforts are beyond the scope of this work, in understanding the effects on the shear stress of the finite probe length, linear and non-linear finite element models simulating conditions similar to those present in the sensor layer during testing were carried out. For example, shear stress contours obtained from linear simulations using the in-house DENDRO software are shown in Fig. 6. In the above figure, three different cases are reported. In Fig. 6a, the half length L of the contact probe is taken to be comparable to the layer thickness H. In Fig. 6b, L is taken to be about half the height H of the layer whereas in Fig. 6c L is taken to be over three times the layer height. In all cases, the areas of zero shear stress are shaded in black whereas the maximum shear stress values are represented by the red shaded

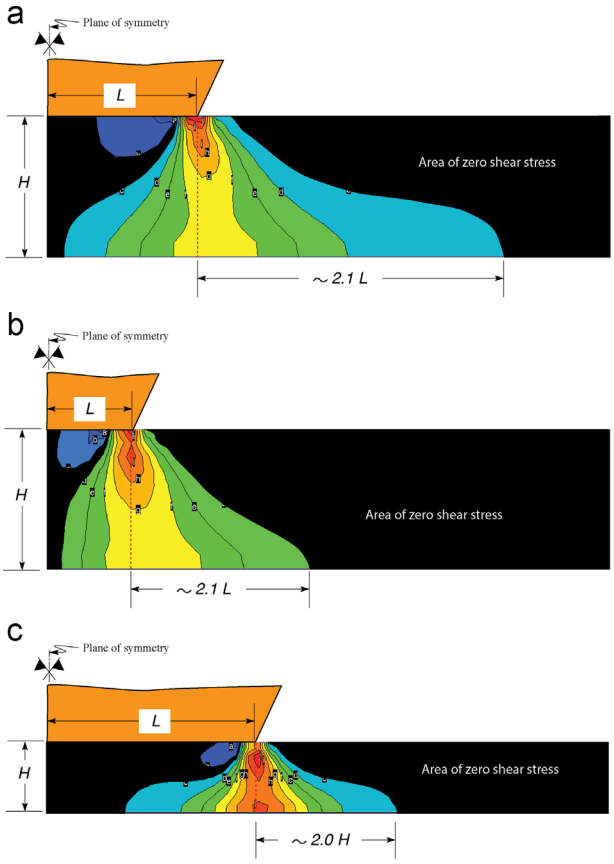

Fig. 6. In-plane shear stress contours developed in a deformable layer, fixed along its bottom surface and subjected to a uniform displacement in the layer contact probe region L. The results are presented for qualitative purposes and were obtained using linear finite elements with the aid of the in-house DENDRO software. (For interpretation of the references to color in this figure caption, the reader is referred to the web version of this paper.)

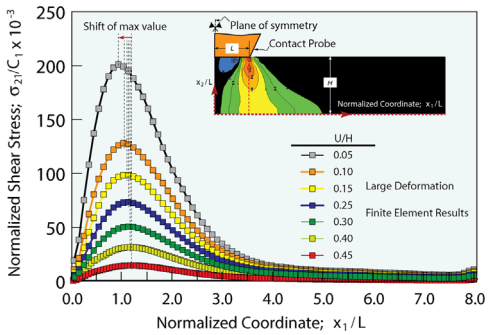

Fig. 7. Profiles of the Cauchy shear stress acting along the fixed edge of a soft polymeric layer subjected to uniform displacement along the contact probe length L. A Mooney–Rivlin material model was used. The large deformation solutions were obtained for different U/H levels using the Abaqus software.

zones. In all three simulations, the shear stress at the symmetry plane is zero as expected. It then increases to a maximum in a region directly below the corner of the contact probe and then it diminishes again to zero at a distance about two times the characteristic length which is smaller of the two lengths present in the problem, i.e., the layer height H or the contact probe half length L. In order to further understand the shear stress effects in adjusting the infinite layer stress solutions, non-linear finite element models using a Mooney–Rivlin material were also carried out with a contact probe being a fourth of the layer thickness. The Cauchy shear stress acting along the fixed bottom surface was then extracted as needed to establish the respective profiles at different layer compression levels. The resulting shear stress profiles are shown in Fig. 7. As shown, for all U/H levels, the shear stresses are zero at the symmetry plane. Consistent with the analytical model, the stresses rise monotonically with x_1 reaching a peak value at distances from the symmetry plane of approximately 2 to 3L. The stresses then fall following what appears to be a Weibull distribution function. For this study, the importance of the profiles reported in Fig. 7 is in identifying an appropriate length L over which the known analytical solutions need to be integrated in enforcing force equilibrium associated with Eq. (43). This is an important aspect of the development of the capacitance model since during experiments the applied force capacitance change relations are reported. The proper estimation of the length over which the analytical shear stress predictions are integrated leads to a relevant value B which in turn controls the pressure and thus the actual value of the normal stresses developed in the layer, and thus the related contact force F.

3. Finite element model development

A non-linear kinematics and material finite element model is developed in parallel to the development of the analytical model for comparison and validation purposes. In doing so, the commercial Finite Element software, Abaqus was used. Abaqus provides state-of-the-art capabilities in modeling hyperelastic materials such as rubber and other isotropic elastomers and offers advanced computational capabilities to solve related models [40]. As will be discussed later on in this section, special care must be given in enforcing incompressibility associated with the behavior of elastomeric materials.

In accordance with the Abaqus documentation [41], the standard or explicit solvers can be used in obtaining Abaqus solutions. More details regarding each of the above solvers and their differences can be found in the Abaqus user's manual [41].

In this work, Abaqus/standard was used to solve problems associated with applied normalized deformation U/H of up to 10%. However, for larger applied deformations, i.e., $U/H=15\%, 20\%, 25\%, 30\%, 40\%$ the Abaqus/explicit solver was used as needed to handle numerical difficulties arising due to material incompressibility and large deformations.

3.1. Material definition

Consistent with the analytical model, the same Mooney–Rivlin material model employed in the development of the analytical model is also used in defining the material used in the Abaqus finite element studies. An important aspect of the material definition however is that while Abaqus/standard enforces incompressibility for hyperelastic materials through the use of special hybrid elements, Abaqus/explicit assumes that the material is nearly incompressible [38], thus allowing a small but negligible degree of compressibility for numerical stability and solution convergence. For example, as discussed in [41], an incompressible material is associated with an infinite wave speed thus resulting in an Abaqus/explicit time increment of zero that does not allow for the advancement of the numerical solution. Therefore, a hyperelastic material definition exhibiting small compressibility must be used. In doing so, the bulk behavior of the model may become softer than that of the actual model material [41]. One can control the material incompressibility through the ratio of the initial bulk modulus, K_0, to its initial shear modulus, μ_0. One can also control the material compressibility through Poisson's ratio, ν, which can be expressed as follows:

$$\nu=\frac{3\frac{K_0}{\mu_0}-2}{6\frac{K_0}{\mu_0}+2}, \tag{47}$$

where K_0 and μ_0 are the bulk and shear modulus respectively and are defined previously in Eq. (16). For illustrative purposes Table 2 shows the value of Poisson's ratio for typical ratios of bulk and shear moduli.

The default Abaqus/explicit value for the bulk to shear modulus ratio is $K_0/\mu_0=20$, corresponding to Poisson's ratio of 0.475. Since typical unfilled elastomers have ratios in the range of 1000–10,000 ($\nu=0.4995$ to $\nu=0.49995$) and filled elastomers have ratios in the range of 50–200 ($\nu=0.490$ to 0.497), this default provides appreciably more compressibility compared to most elastomer behavior. However, if the elastomer is relatively unconfined, this softer modeling of the material's bulk behavior usually provides quite accurate results [41].

Instead of accepting the Abaqus/explicit default value, one has the option of defining the material compressibility. When doing so, one should be aware that when using a value for the ratio k_0/μ_0 which is larger than 100, high frequency noise is then introduced into a dynamic solution which then requires the use of excessive small time increments as discussed in [41].

Thus, in determining the shortest time step for quasi-static analysis in Abaqus/explicit, frequency analysis was carried out on the polymeric model used in the study. The study yielded a

Table 2
Poisson's ratio for typical values of K_0/μ_0 [41].

$\frac{K_0}{\mu_0}$	ν
10	0.452
20	0.475
50	0.490
10 0	0.495
1000	0.4995
10,000	0.49995

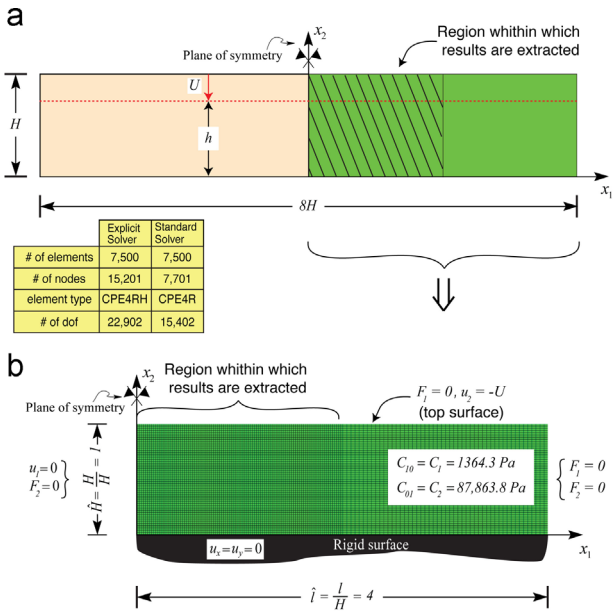

Fig. 8. (a) A schematic of the domain within which a finite element solution is obtained. The highlighted in green right half of the domain is the finite element model region discretized using four-noded hybrid elements for the Abaqus/standard (CPE4RH) solver or four-noded elements (CPE4R) when using the Abaqus/explicit solver. (b) A typical finite element mesh with geometric symmetry, displacement and traction conditions shown. (For interpretation of the references to color in this figure caption, the reader is referred to the web version of this paper.)

fundamental frequency for the polymeric layer to be 3.6177 Hz corresponding to a period of 0.2764 s which is then used as the shortest step time in obtaining the Abaqus/explicit solutions reported in this study.

3.2. Geometry definition and meshing

The finite element solution domain selected for this study is shown in Fig. 8a. As shown the domain has an aspect ratio of height to length $H/L = 1/4$. The above domain is meant to represent the right symmetric half of the compressed layer. This domain was discretized using 4-noded elements. A typical mesh is shown in Fig. 8b. In the above mesh which was created and then processed in Abaqus, there are 7500 quadrilateral, plane-strain, reduced, hybrid elements designated as `CPE4RH` in Abaqus/standard and 7500 quadrilateral, plane-strain, reduced, elements designated as `CPE4R+` in Abaqus/explicit. The mesh in Abaqus/standard also contains 15,201 nodes with a 15,402 displacement degrees of freedom and 7500 additional pressure degrees of freedom (total of 22,902 degrees of freedom) but the mesh in Abaqus/explicit consists of 7701 nodes which correspond to 15,402 degrees of freedom. More specifics of the size of the problem in Abaqus/standard and Abaqus/explicit are included in Fig. 8. Symmetry conditions were applied along the $x_1 = 0$ plane. Fixed displacement conditions were applied along the rigid surface at the bottom of the layer. Free traction conditions were enforced in the x_1 direction on the top surface while a uniform displacement in the negative x_2 direction was applied to all nodes on the top surface of the mesh.

A Mooney–Rivlin material model was adopted as discussed earlier with the material constants $C_1 = 1,364.3$ Pa, $C_2 = 87,863.8$ Pa given as a material input. It may be important to state that the sign of C_{10} is taken to be positive for the Abaqus simulations since in Abaqus the Mooney–Rivlin stress law includes a negative sign ahead of the respective C_{10} constitutive term [41] whereas the same term is used with a positive sign in the analytical model consistent with Eq. (17). Incompressibility condition was also enforced by choosing Poisson's ratio to be close to 0.5.

The Abaqus models were run using an Intel (R) Core (TM)2 Duo CPU P8600 at 2.4 GHz with typical run execution times of the order of 4000 s. An incremental and iterative scheme was used in obtaining the solutions at all deformation levels reported.

For numerical verification purposes the same FE models solved in Abaqus were also solved using the COMSOL multiphysics [42].

4. Results and discussion

The aim of the broad parametric studies presented below is twofold; (a) the studies allow us for the comparison of the analytical model predictions to independent estimates obtained using the Method of Finite Elements over a broad range of layer compression and (b) the parametric studies allow us for the determination of the stress and deformation fields induced in the layer by the application of a uniform displacement at the top layer surface under large deformation condition. The applied displacement loading is meant to simulate sensor contact at the top layer surface. As such, the results presented below are sequentially organized consistent with the level of layer compression. Results for two layer compression simulations are presented, i.e., $U/H = 0.05$ and 0.4. Within each layer compression simulation, the reported results include Cauchy stress profiles along the x_1 at various fixed x_2 positions and the same stress plotted along the x_2 at fixed various x_1 positions. In addition, the results include displacement profiles along the x_1 and x_2 directions as needed to fully explore the model capabilities and elucidate the large deformation mechanics dominating the layer under consideration. The figures presented in this study include both analytical model predictions plotted in solid lines and finite element results denoted by discrete points presented in the same plots.

In all finite element simulations, the geometry was normalized with respect to the layer thickness H which was used as the characteristic length in the model. In addition, the applied displacement was normalized with respect to H and as such it was imposed as a displacement condition using the ratio of the applied displacement U over the layer thickness H as indicated above. However, as mentioned earlier in Section 3, the finite element simulations were initially carried out using a dimensional Mooney–Rivlin material with constants $C_{01} = 1364.3$ Pa and $C_{10} = -87,863.8$ Pa. The non-dimensionilization of the finite element stress results with respect to the constant C_{01} was then performed after the extraction of the initial dimensional data as needed to establish consistency between the reported finite element data and those obtained using the analytical model. It may also be important to state that the results obtained using the analytical model developed earlier in this work were non-dimensionalized using the non-dimensionilization process discussed earlier in this study. In light of all of the above, the simulation results shall be discussed next.

Figs. 9–11 report on stress and deformation results obtained for a layer subjected to a normalized displacement $U/H = 0.05$ applied along the top layer surface. More specifically, Fig. 9 shows profiles of the non-dimensional Cauchy stress components plotted against the normalized x_1/H coordinate for various fixed values of x_2/H. Fig. 9a reports on the normalized σ_{11}/C_1 Cauchy stress component, Fig. 9b on the normalized σ_{22}/C_1 shear component and Fig. 9c on the normalized σ_{12}/C_1 Cauchy stress component. In all figures, the solid lines represent analytical model predictions whereas the discrete points correspond to finite element results. Each set of results reported in solid line and related FE points were obtained at a fixed normalized layer depth as measured by the

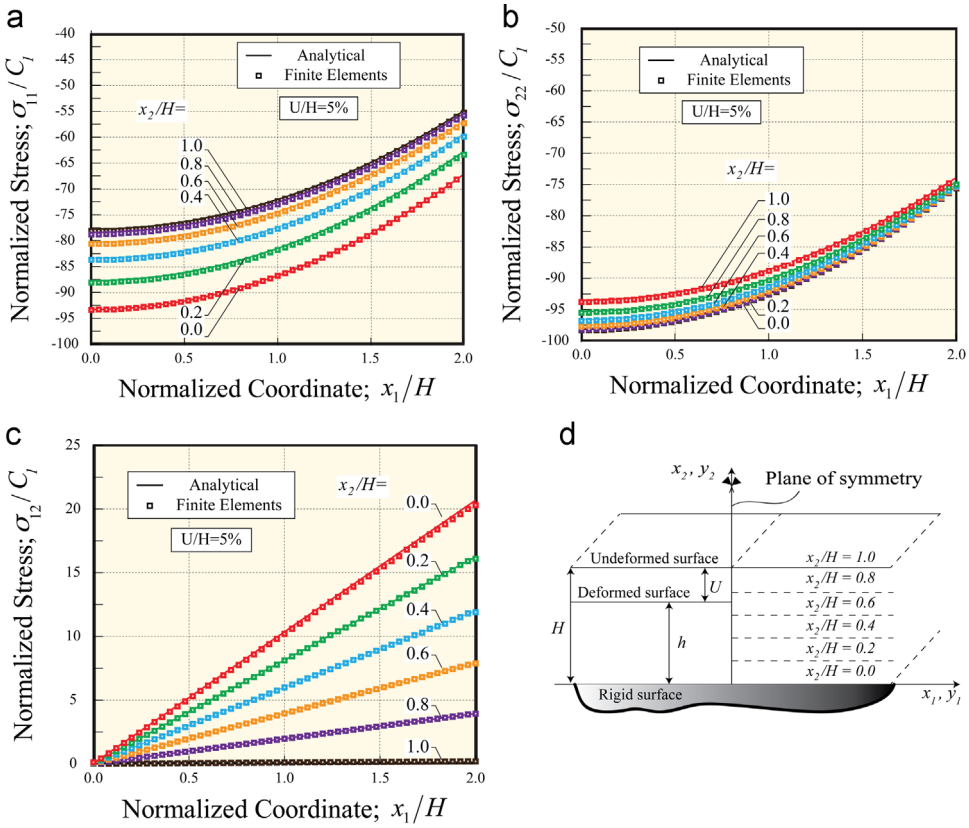

Fig. 9. Profiles of non-dimensional Cauchy stress components (a) $\hat{\sigma}_{11}$, (b) $\hat{\sigma}_{22}$, (c) $\hat{\sigma}_{12}$ plotted against the non-dimensional reference coordinate $\hat{x}_1$ at different $\hat{x}_2$ cross sections as indicated, for an applied compressive normalized displacement, $U/H = 0.05$. The discrete points represent Abaqus/standard, finite element results whereas the solid lines represent the analytical model predictions. (d) Schematic of the polymeric layer subjected to a compressive uniform displacement U. The horizontal dash lines represent the paths of the reported stress profiles.

parameter x_2/H as indicated in the accompanied schematic in Fig. 9d. As shown, the analytical predictions for all three stress components are in excellent agreement with the finite element results. Despite the relatively modest level of layer compression, i.e., 5% thickness reduction, the observed agreement between the analytical and finite element results can be seen as a validation of both the analytical and the numerical finite element models developed in this study. As discussed later on in this section, further validation of the two modeling approaches is established at much higher layer compression reaching up to a severe 40% thickness reduction.

It may also be important to note that under the applied layer compression condition, both normal Cauchy stresses, i.e., σ_{11} and σ_{22}, are predicted to be in compression over the entire range of the reported data, i.e., with x_1/H varying from 0 to 2 and at all normalized layer depths reported. Higher compression levels appear to exist in the vicinity of the symmetry plane with σ_{11}/C_1 being close to -93 at a material point at the bottom of the layer on the symmetry axis and σ_{22}/C_1 being equal to -98 at the same point. As shown in Fig. 9c, all shear stresses at the symmetry plane vanish consistent with symmetry condition and increase linearly with x_1/H with the higher rate of increase associated with material points attached to the rigid substrate. Again, as expected, all shear stresses vanish at the friction free top surface.

In Fig. 10, the normalized Cauchy stress component profiles at fixed distances from the symmetry plane as measured by x_1/H are plotted against the normalized x_2/H coordinate for top surface compression $U/H = 0.05$ as mentioned earlier. Again, the solid lines represent analytical model predictions and discrete points those obtained numerically using finite elements. Consistent with the simulations presented in Fig. 9, the results shown in Fig. 10 maintain the remarkable agreement between the analytical and FE model predictions. While the normalized σ_{11}/C_1 stress appears to exhibit a non-linear profile with x_2/H, the σ_{22}/C_1 is shown to remain almost constant along the layer depth whereas the shear stresses appear to linearly decrease from a maximum at the bottom of the layer to zero at the top of the layer.

The profiles of the displacement components u_1/H and u_2/H plotted along horizontal lines of fixed x_2/H are shown in Figs. 11a and 11c. As expected, the normalized u_2/H displacement component is shown to be independent of x_1 as shown in Fig. 11c, it is also predicted to be equal to the applied displacement for material points on the top layer surface and zero for points attached to the rigid foundation. On the contrary, the normalized u_1/H component, the component that is relevant to the pressure sensor design, is shown to be zero on the symmetry axis and then increases linearly with x_1/H for points belonging to the same horizontal line at fixed distance x_2/H from the rigid bottom. As will be discussed later on, in [2] in the pressure sensor capacitance model development, higher u_1 components lead to higher sensor capacitance change which may increase sensor sensitivity. Of course, other sensor design issues at play often necessitate minimizing the distance between electrodes limiting the electrode placement to distances from the axis of symmetry to $x_1 < 0.2H$ as will be further investigated in [2].

The u_1/H and u_2/H displacement component profiles plotted against x_2/H along vertical lines of constant x_1/H are shown in Figs. 11b and 11d respectively. Fig. 11b indicates that the u_1/H exhibit a non-linear profile when plotted along a vertical line. As expected, higher values for u_1/H are predicted for vertical lines located further from the symmetry plane as needed for conservation of mass. As discussed above, the trends in u_1/H in either x_1/H

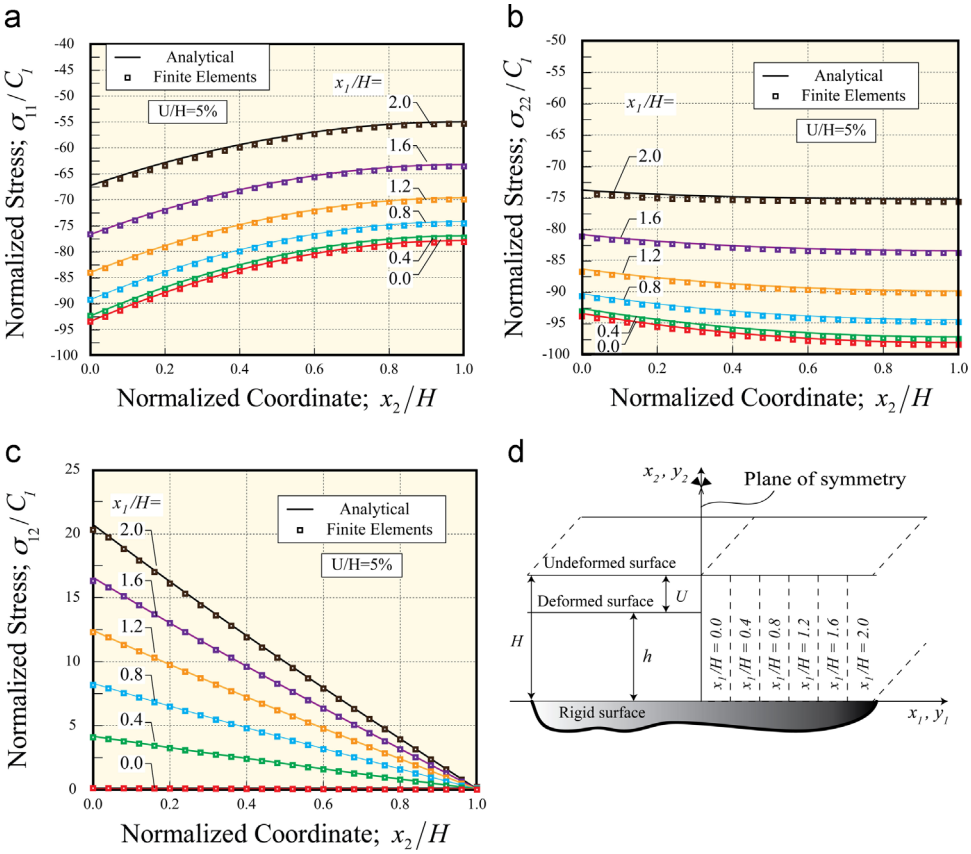

Fig. 10. Profiles of the non-dimensional Cauchy stress components (a) $\hat{\sigma}_{11}$, (b) $\hat{\sigma}_{22}$, (c)$\hat{\sigma}_{12}$ plotted against the non-dimensional reference coordinate $\hat{x}_2$ at different $\hat{x}_1$ locations. The results were obtained for an applied compressive normalized displacement, $U/H = 0.05$. The discrete points represent Abaqus/standard, finite element results whereas the solid lines represent the analytical model predictions. (d) Schematic of the polymeric layer subjected to a compressive uniform displacement U. The vertical dash lines represent the paths of the reported stress profiles.

reported in Fig. 11a or x_2/H reported in Fig. 11b are of relevance to pressure sensor design and thus, the profiles shown in the latter figure could assist in the development of optimal designs. The profile of u_2/H along vertical lines reported in Fig. 11d further reinforces our understanding of its independence of x_1/H as assumed in the analytical model development. As shown, the reported profiles for all x_1/H lines coincide forming a single profile. Zero u_2/H displacements are predicted for all points along the rigid bottom whereas points on the top surface experience u_2/H equal to the applied displacement. A non-linear profile is exhibited by the u_2/H component between points on the bottom rigid surface and points on the top layer surface.

Stress and displacement profiles similar to those presented in Figs. 9 and 11 are also obtained for the most severe layer compression case of $U/H = 0.40$ considered herein and reported in Figs. 12 and 13. More specifically, Fig. 12 shows the normalized Cauchy stress components $\hat{\sigma}_{11}, \hat{\sigma}_{22}, \hat{\sigma}_{12}$, and the normalized displacement components $\hat{u}_1, \hat{u}_2$ extracted along horizontal paths plotted against the non-dimensional reference coordinates $\hat{x}_1$ at different $\hat{x}_2$ cross sections. At the same time, Fig. 13 shows the normalized displacement components $\hat{u}_1$ and $\hat{u}_2$ extracted along vertical paths and plotted against the normalized reference coordinates $\hat{x}_2$ at different $\hat{x}_1$ fixed vertical paths. While a broad array of results similar to those reported for the 5% layer compression case were also obtained for the 40% compression, in an effort to limit the extend of this paper, only selected but still sufficiently comprehensive results are included for the latter case asreported in Figs. 12 and 13.

As evident by the results reported in Figs. 9–13, the stress and deformation profile trends obtained for the higher levels of layer compression are shown to be similar to the corresponding trends exhibited and discussed for the 5% layer compression. Overall, the analytical model predictions are shown to be in remarkable agreement with the finite element results for all layer compression levels considered with slight deviations appearing in the most severe case of 40% layer compression. Again, by inspection one recognizes that higher compressive stresses develop with increasing layer compression with the normalized σ_{11}/C_1 at the bottom of the layer on the symmetry plane being close to 93 for the 5% layer compression case (see Fig. 9a), increasing to an astonishing high value of about 3500 for the severe 40% layer compression case as shown in Fig. 12a.

An important finding of the above discussed parametric studies is the observed agreement between the analytical and finite element models for modest as well as severe layer compression levels. Such a finding reinforces confidence in the analytical model capabilities which can be used to develop a related sensor capacitance model and thus guide the optimal design of pressure sensors.

5. On the development of a sensor capacitance model

The layer compression model developed above is employed in a separate study [2] in the development of an all elastomer tactile MEMS sensor for the detection of contact forces. A schematic of the MEMS pressure sensor developed in [1] is shown in Fig. 14. As shown, through a special micro-fabrication process, conductive layers are embedded into an otherwise soft polymeric layer of initial thickness H. In [1], pressure sensor devices of layer thickness

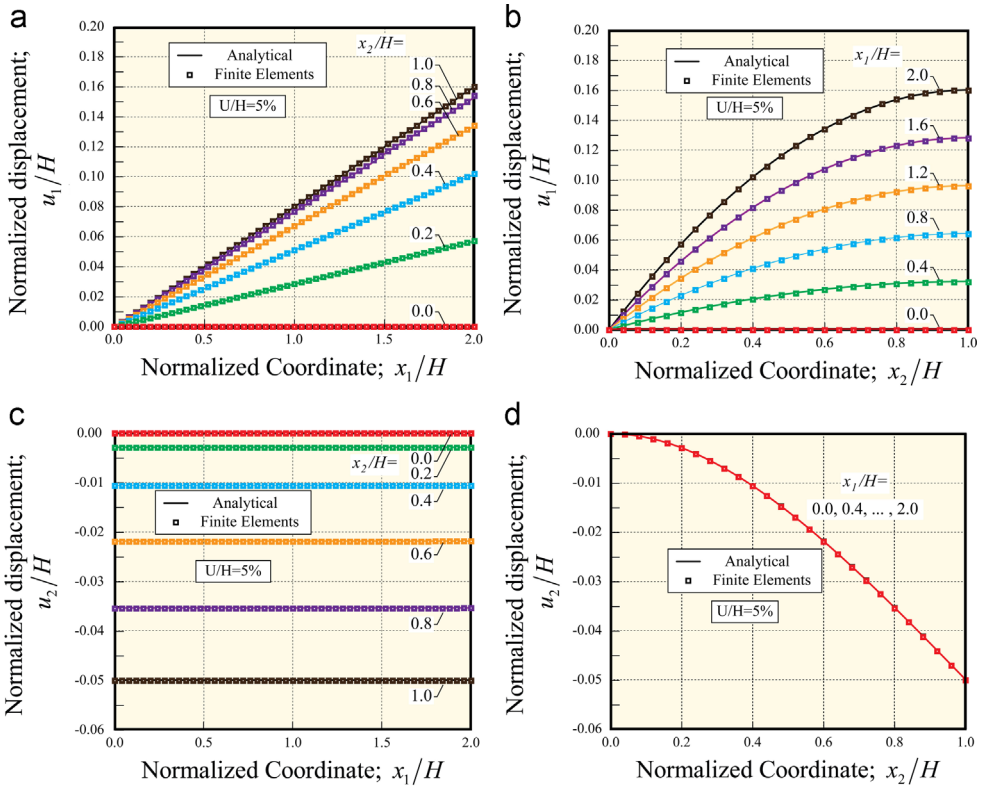

Fig. 11. Profiles of the non-dimensional displacement components extracted along horizontal and vertical paths. (a) $\hat{u}_1$ plotted against $\hat{x}_1$ at different $\hat{x}_2$-fixed horizontal paths. (b) $\hat{u}_1$ plotted against $\hat{x}_2$ at different $\hat{x}_1$-fixed vertical paths. (c) $\hat{u}_2$ plotted against $\hat{x}_1$ at different $\hat{x}_2$-fixed horizontal paths. (d) $\hat{u}_2$ plotted against $\hat{x}_2$ at different $\hat{x}_1$-fixed vertical paths. The discrete points represent Abaqus/standard, finite element results whereas the solid lines represent the analytical model predictions. The reported results were obtained for an applied compression $U/H=0.05$.

$H=450$ μm were developed and tested. Upon contact, the soft polymeric layer compresses to a smaller thickness h while at the same time displacing material symmetrically outwards from the center of contact consistent with Fig. 15a. Thus, the initial electrode spacing D increases to a larger spacing d while also the electrode layer thickness reduces from an initial thickness T to a current thickness t. Consistent with the flowchart included in the Fig. 15b, the capacitance C which is proportional to the initial electrode overlapping area A_o and inversely proportional to the current electrode distance d changes during contact. Such changes can then be measured with proper sensor calibration thus identifying the magnitude of the applied contact force as a function of capacitance change. Thus, in doing so and consistent with Fig. 15, the relationship between the applied displacement U/H and the resulting contact pressure or associate contact force F needs to be established using the analytical model developed earlier in this study.

5.1. Force–displacement curves

The total force acting in the sensor contact region can be calculated using the contact surface stresses predicted by the analytical model. Particularly, under plane strain conditions for a sensor of width w, the total force acting over an undeformed area of length $2L_C \times w$ is given by

$$F = 2\int_0^{L_c} T_{22}(x_1, x_2 = H)w\, dx_1, \tag{48}$$

where F is the total force applied to the contact area, $T_{22}(x_1, x_2 = H)$ is the 1st Piola–Kirchhoff stress component normal to the top surface of the layer, w is the layer width, L_c is half of the length of contact length and x_1 is a reference coordinate. The same force can also be obtained by integrating the corresponding Cauchy stress component σ_{22} over the deformed area. Consistent with the above configuration, if initial contact is made over the $2L_c \times w$ area and provided that contact is maintained over the deformed area $2L_c' \times w$, then the total force is given by

$$F = 2\int_0^{L_c'(U)} \sigma_{22}(y_1, y_2 = H)w\, dy_1. \tag{49}$$

With the aid of the analytical model stress predictions the above force displacement equation takes the form

$$F = 2w\lambda L\left(-\frac{\mu_0}{6}AL^2\lambda^2 + \frac{\mu}{2}\frac{1}{\lambda^2} - B\right) \tag{50}$$

and it can be normalized as

$$\hat{F} = \frac{F}{\mu_0 H^2} = 2\hat{w}\hat{\lambda}\hat{L}\left(-\frac{\hat{\mu}_0}{6}\hat{A}\hat{L}^2\hat{\lambda}^2 + \frac{\hat{\mu}_0}{2}\frac{1}{\hat{\lambda}^2} - \hat{B}\right) \tag{51}$$

where C_1, C_2 are the Mooney–Rivlin material constants, $\mu_0 = C_1 - C_2$ is the shear modulus of the polymeric layer, $\lambda(\alpha)$ is a function given by Eq. (36), A is a constant which is equal to $-\alpha^2$, Eq. (34), and α is a constant that solely depends on the layer compression level U/H and is calculated numerically by solving a non-linear expression given by Eq. (39). A list of α values for various U/H ratios is given in Table 1. As discussed earlier on, in Section 2.7, "hat" quantities are non-dimensionalized with their characteristic values.

Typical profile of normalized contact force plotted against U/H is presented in Fig. 16. As shown, a highly non-linear relationship exists between the uniform layer compression U/H and the normalized contact force applied over a specified initial length L.

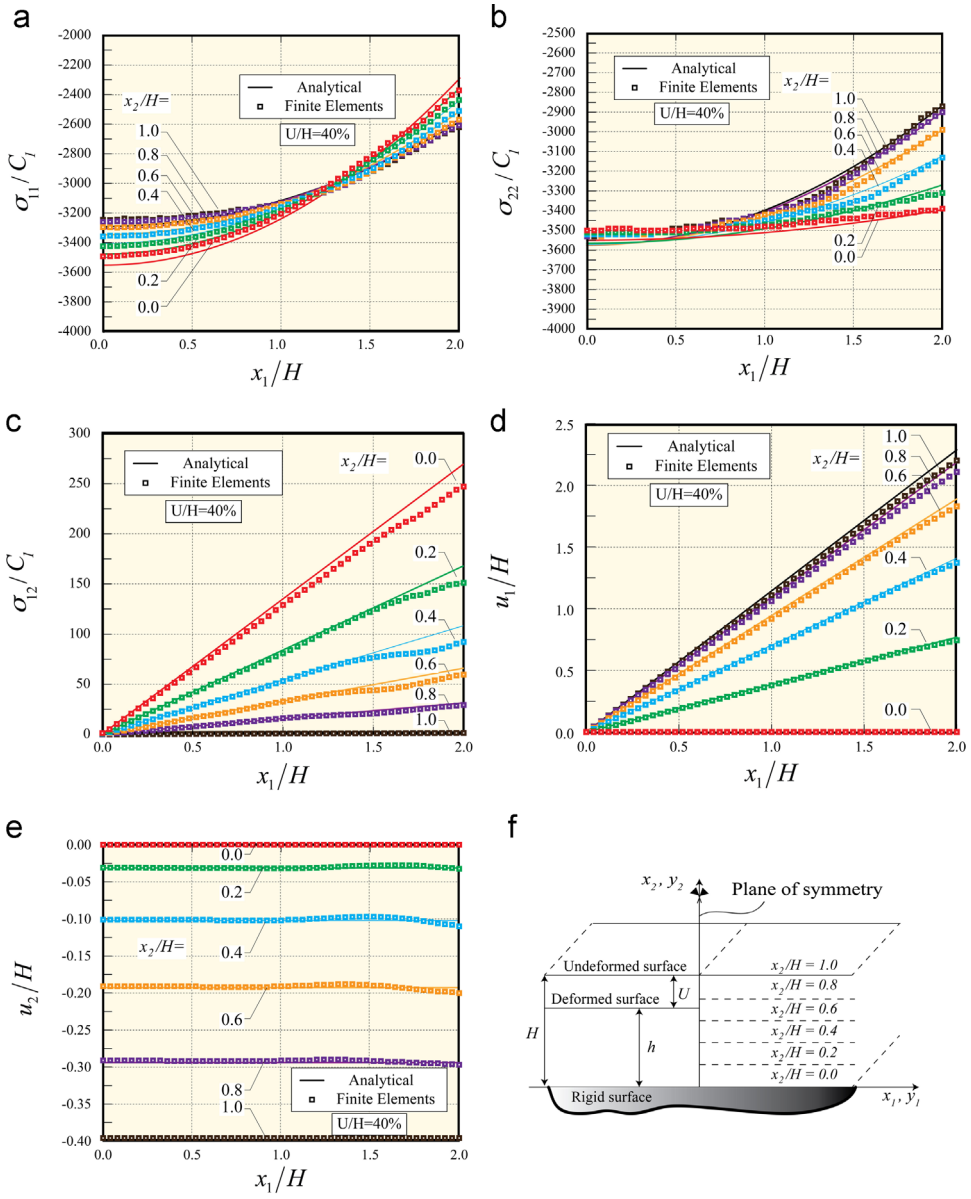

Fig. 12. Profiles of the non-dimensional (a) Cauchy stress component $\hat{\sigma}_{11}$, (b) Cauchy stress component $\hat{\sigma}_{22}$, (c) Cauchy stress component $\hat{\sigma}_{12}$, (d) displacement component $\hat{u}_1$, (e) displacement component $\hat{u}_2$, extracted along horizontal paths plotted against the non-dimensional reference coordinate $\hat{x}_1$ at different $\hat{x}_2$ cross sections as indicated and consistent with schematic of the polymeric layer subjected to a compressive uniform displacement U in (f). The discrete points represent Abaqus/explicit, finite element results whereas the solid lines represent the analytical model predictions. The results are obtained for applied compressive normalized displacement $U/H = 0.40$.

The value of the force resultant $\hat{F}$ clearly depends on the constant $\hat{B}$. The sensor model calibration leading to a relevant constant $\hat{B}$ is discussed in great detail in [2].

6. Conclusions

The large deformation mechanics of a soft, planar and infinitely long elastomeric layer subjected to a uniform compressive displacement have been established both analytically and numerically using the Method of Finite Elements (FEM). An incompressible Mooney–Rivlin material model was employed with the layer subjected to the uniform displacement under plane strain conditions. In the analytical model development, the Cauchy stress tensor was expressed in terms of an independent spatially varying pressure term, the Finger deformation tensor and its inverse each multiplied by a Mooney–Rivlin material constant. Material incompressibility along with geometric boundary conditions, local stress and global force equilibrium have been used in establishing explicit forms of the large deformation kinematic equations. Thus analytical expressions for the true or Cauchy stresses and the 1st Piola–Kirchhoff stresses have been obtained. Similarly, analytical expressions for the in-plane displacement components have also been developed. Analytical stress and deformation estimates in the region close to the symmetry plane along with their finite element counterparts are reported for relatively as well as severe applied deformation of up to 40% of the original layer thickness. The analytical predictions are found to be in remarkable agreement with their finite element counterparts. The relevance of the analytical model to the development of a tactile sensor capacitance model is discussed. Contact force profiles plotted against the applied displacement over a finite contact probe length are also reported.

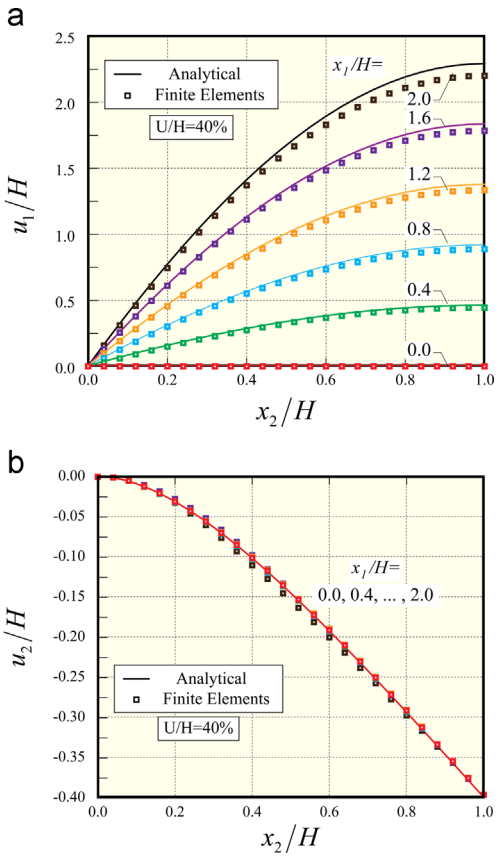

Fig. 13. Profiles of the non-dimensional displacement components extracted along vertical paths. (a) $\hat{u}_1$ plotted against $\hat{x}_2$ at different $\hat{x}_1$-fixed vertical paths. (b) $\hat{u}_2$ plotted against $\hat{x}_2$ at different $\hat{x}_1$-fixed vertical paths. The discrete points represent Abaqus/explicit, finite element results whereas the solid lines represent the analytical model predictions. The reported results were obtained for an applied compression $U/H = 0.40$.

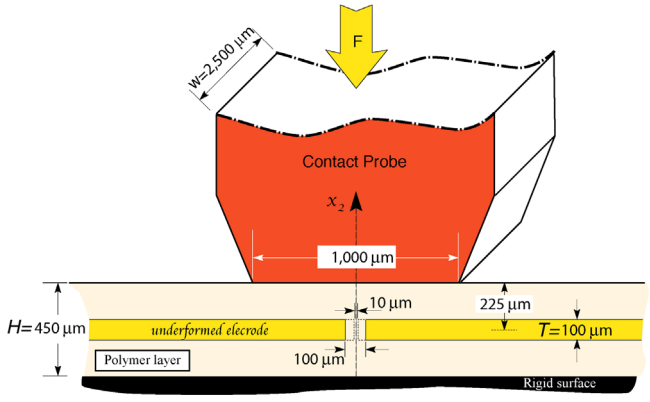

Fig. 14. A schematic showing the geometry of the MEMS pressure sensor fabricated and tested in [1] along with the contact probe used in the sensor capacitance testing. It may be of importance to note that the aspect ratio of the contact probe to electrode gap ratio varies from a low of 10 for electrode gap of 100 µm to 100 for electrode gap of 10 µm. In either cases, the infinitely long layer model used in the development of the analytical model is justified since only the mechanics in the vicinity of the electrode gap is used in the capacitance model.

The model developed in this work forms the foundation for the development of a robust capacitance model for pressure tactile sensor applications.

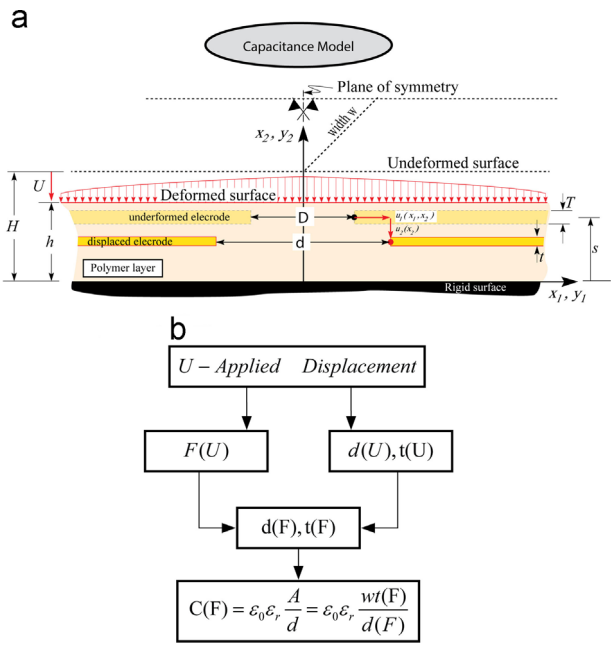

Fig. 15. (a) A schematics of the MEMS pressure sensor developed in [1] and modeled in this study. (b) A flow chart indicating the process used to establish the relationship between the sensor capacitance $C(F)$ and the applied contact force F developed in [2].

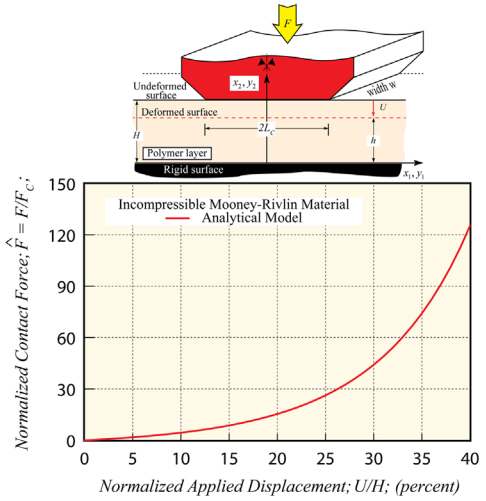

Fig. 16. The normalized contact force calculated over a prescribed length L_c, plotted against the percentage of layer thinning as measure by the applied displacement U/H. In normalizing the contact force reported above, $F_c = \mu_0 H^2$. The analytical simulations were carried out for a soft polymeric layer modeled using a Mooney–Rivlin material with $C_1 = 1364.3$ Pa and $C_2 = -87,863.8$ Pa.

Acknowledgments

This work was inspired by the research reported in [1]. The authors are grateful to useful and insightful conversations and feedback with the authors of [1]; Dr. *Sarah Bergbreiter* and Ph.D. student Mr. *Alexi Charalambides*.

References

[1] A. Charalambides, S. Bergbreiter, All-elastomer in-plane MEMS capacitive tactile sensor for normal force detection, in: 2013 IEEE Sensors, 2013, pp. 1–4.
[2] K.M. Kalayeh, A.G. Charalambides, S. Bergbreiter, P.G. Charalambides, Predicting the response of an all-elastomer in-plane MEMS tactile sensor, In preparation (2015).

[3] S. Jacobsen, I. McGammon, K. Biggers, R. Phillips, Design of tactile sensing systems for dextrous manipulators, IEEE Control Syst. Mag. 8 (1) (1988) 3–13.
[4] J.L. Novak, Initial design and analysis of a capacitive sensor for shear and normal force measurement, in: Proceedings of 1989 IEEE International Conference on Robotics and Automation, vol. 1, 1989, pp. 137–144.
[5] F. Zhu, J.W. Spronck, A capacitive tactile sensor for shear and normal force measurements, Sens. Actuators A: Phys. 31 (1–3) (1992) 115–120.
[6] T.A. Chase, R. Luo, A thin-film flexible capacitive tactile normal/shear force array sensor, in: Proceedings of the 1995 IEEE IECON 21st International Conference on Industrial Electronics, Control, and Instrumentation, vol. 2, 1995, pp. 1196–1201.
[7] J. Dargahi, S. Najarian, Advances in tactile sensors design/manufacturing and its impact on robotics applications—a review, Ind. Robot: Int. J. 32 (3) (2005) 268–281.
[8] R.S. Dahiya, G. Metta, M. Valle, G. Sandini, Tactile sensing—from humans to humanoids, IEEE Trans. Robot. 26 (1) (2010) 1–20.
[9] K.F. Lei, K.-F. Lee, M.-Y. Lee, Development of a flexible PDMS capacitive pressure sensor for plantar pressure measurement, Microelectron. Eng. 99 (2012) 1–5.
[10] T. Zhang, H. Liu, L. Jiang, S. Fan, J. Yang, Development of a flexible 3-d tactile sensor system for anthropomorphic artificial hand, IEEE Sens. J. 13 (2) (2013) 510–518.
[11] Y. Su, R. Li, H. Cheng, M. Ying, A.P. Bonifas, K.C. Hwang, J.A. Rogers, Y. Huang, Mechanics of finger-tip electronics, J. Appl. Phys. 114 (16) (2013) 164–511.
[12] G. Cannata, M. Maggiali, G. Metta, G. Sandini, An embedded artificial skin for humanoid robots, in: IEEE International Conference on Multisensor Fusion and Integration for Intelligent Systems, MFI 2008, Seoul, Korea, IEEE, 2008, pp. 434–438.
[13] T. Hoshi, H. Shinoda, Robot skin based on touch-area-sensitive tactile element, in: Proceedings of 2006 IEEE International Conference on Robotics and Automation, ICRA 2006, 2006, pp. 3463–3468.
[14] P. Puangmali, K. Althoefer, L. Seneviratne, D. Murphy, P. Dasgupta, State-of-the-art in force and tactile sensing for minimally invasive surgery, IEEE Sens. J. 8 (April) (2008) 371–381.
[15] A. Mirbagheri, S. Najarian, J. Dargahi, F.T. Ghomshe, Mathematical modeling of a tactile sensor with applications in minimally invasive surgery, Am. J. Appl. Sci. 4 (10) (2007) 779–785.
[16] M.H. Lee, H.R. Nicholls, Review article tactile sensing for mechatronics—a state of the art survey, Mechatronics 9 (1) (1999) 1–31.
[17] D. Zhou, H. Wang, Design and evaluation of a skin-like sensor with high stretchability for contact pressure measurement, Sens. Actuators A: Phys. 204 (2013) 114–121.
[18] M.Y. Cheng, C.L. Lin, Y.T. Lai, Y.J. Yang, A polymer-based capacitive sensing array for normal and shear force measurement, Sensors 10 (11) (2010) 10211–10225.
[19] R.D. PonceWong, J.D. Posner, V.J. Santos, Flexible microfluidic normal force sensor skin for tactile feedback, Sens. Actuators A: Phys. 179 (2012) 62–69.
[20] M.Y. Cheng, X.H. Huang, C.W. Ma, Y.J. Yang, A flexible capacitive tactile sensing array with floating electrodes, J. Micromech. Microeng. 19 (11) (2009) 115001.
[21] E.S. Hwang, J.-h. Seo, Y.J. Kim, A polymer-based flexible tactile sensor for both normal and shear load detections and its application for robotics, J. Microelectromech. Syst. 16 (3) (2007) 556–563.
[22] L. Wang, D.J. Beebe, A silicon-based shear force sensor: development and characterization, Sens. Actuators A: Phys. 84 (1) (2000) 33–44.
[23] D.J. Beebe, D.D. Denton, R.G. Radwin, J.G. Webster, A silicon-based tactile sensor for finger-mounted applications, IEEE Trans. Biomed. Eng. 45 (2) (1998) 151–159.
[24] J.H. Shan, T. Mei, L. Sun, D.Y. Kong, L. Ni, M. Meng, J.R. Chu, The design and fabrication of a flexible three-dimensional force sensor skin, in: 2005 IEEE/RSJ International Conference Edmonton, Alberta, Canada. IEEE, 2005, pp. 1818–1823.
[25] F. Jiang, G.B. Lee, Y.C. Tai, C.M. Ho, A flexible micromachine-based shear-stress sensor array and its application to separation-point detection, Sens. Actuators A: Phys. 79 (3) (2000) 194–203.
[26] H.K. Lee, S.I. Chang, E. Yoon, A flexible polymer tactile sensor: fabrication and modular expandability for large area deployment, J. Microelectromech. Syst. 15 (6) (2006) 1681–1686.
[27] H.-K. Lee, J. Chung, S.-I. Chang, E. Yoon, Normal and shear force measurement using a flexible polymer tactile sensor with embedded multiple capacitors, J. Microelectromech. Syst. 17 (4) (2008) 934–942.
[28] E. Pritchard, M. Mahfouz, B. Evans, S. Eliza, M. Haider, Flexible capacitive sensors for high resolution pressure measurement, in: 2008 IEEE Sensors, 2008, pp. 1484–1487.
[29] J. da Rocha, P. da Rocha, S. Lanceros-Mendez, Capacitive sensor for three-axis force measurements and its readout electronics, IEEE Trans. Instrum. Meas. 58 (8) (2009) 2830–2836.
[30] S. Kumar, G. Liu, M. Srinivasan, Flexible membrane tactile sensor for contact traction distribution measurement on a microscale, in: World Haptics Conference (WHC), June, 2011, Istanbul, Turkey. IEEE, 2011, pp. 627–632.
[31] A. D'Amore, G. DeMaria, L. Grassia, C. Natale, S. Pirozzi, Silicone-rubber-based tactile sensors for the measurement of normal and tangential components of the contact force, J. Appl. Polym. Sci. 122 (6) (2011) 3757–3769.
[32] G. De Maria, C. Natale, S. Pirozzi, Force/tactile sensor for robotic applications, Sens. Actuators A: Phys. 175 (2012) 60–72.
[33] G. De Maria, C. Natale, S. Pirozzi, Tactile data modelling and interpretation for stable grasping and manipulation, Robot. Auton. Syst., 2013.
[34] H.K. Lee, J. Chung, S.I. Chang, E. Yoon, Real-time measurement of the three-axis contact force distribution using a flexible capacitive polymer tactile sensor, J. Micromech. Microeng. 21 (3) (2011) 035010.
[35] G. Liang, D. Mei, Y. Wang, Z. Chen, Modeling and analysis of a flexible capacitive tactile sensor array for normal force measurement, Sens. J. IEEE 14 (November) (2014) 4095–4103.
[36] D.J. Cohen, D. Mitra, K. Peterson, M.M. Maharbiz, A highly elastic, capacitive strain gauge based on percolating nanotube networks, Nano Lett. 12 (4) (2012) 1821–1825.
[37] W.W. Klingbeil, R.T. Shield, Large-deformation analyses of bonded elastic mounts, Z. für angew. Math. Phys. 17 (2) (1966) 281–305.
[38] Some applications of elasticity theory to rubber engineering, in: Collected Papers of RS Rivlin, Springer, 1997, pp. 9–16. Also presented at the Rubber Technology Conference, London, England, June 23rd to 25th, 1948.
[39] A. Ali, M. Hosseini, B.B. Sahari, A review of constitutive models for rubber-like materials, Am. J. Eng. Appl. Sci. 3 (1) (2010) 232.
[40] M.R. Gurvich, A constitutive model of hyperelastic anisotropic materials: approach and implementation in ABAQUS, in: Proceedings of the 2004 ABAQUS Users' Conference, 2004, pp. 281–289.
[41] S.I. Habbit, Karlsson, ABAQUS Documentation, Dassault Systèmes, RI, USA, 2013.
[42] Comsol multiphysics modeling software. ⟨http://www.comsol.com⟩, (Visited on 14/04/2015).